





Cite this: DOI: 10.1039/d1ta09795d

A smart flexible supercapacitor enabled by a transparent electrochromic electrode composed of $W_{18}O_{49}$ nanowires/rGO composite films†

Muhammad Hassan,^a Ghulam Abbas,^a Yao Lu,^b Ziya Wang *^{ac} and Zhengchun Peng *^a

In this study, we fabricated a transparent conductive electrode by co-assembly of Ag and $W_{18}O_{49}$ nanowires, followed by the deposition of several $W_{18}O_{49}$ NWs/rGO composite layers. The as-fabricated transparent electrode exhibits tunable transmittance (72–84% at 550 nm) and a conductivity of 23–39 Ω sq^{-1} . Noteworthy, the hybrid film structure made of 15 layers of $W_{18}O_{49}$ NWs/rGO composite reveals an areal capacitance of 92 $mF\ cm^{-2}$ with a fast and reversible switching response. The electrode can sustain an optical modulation of 94.7% even at a high current density of 10 $mA\ cm^{-2}$. Furthermore, the electrode exhibits excellent electrochromic performance with fast switching speeds (8 s for coloration and 8.45 s for bleaching), high colouration efficiency (46 $cm^2\ C^{-1}$) and remarkable stability (96.41% of the original optical modulation). A smart bifunctional electrochromic supercapacitor based on this electrode demonstrates a maximum areal capacitance of 48 $mF\ cm^{-2}$ and an energy density of 5.2 $\mu W\ h\ cm^{-2}$ with 0.391 $mW\ cm^{-2}$ power density. The device shows excellent mechanical flexibility and stability over 4000 cycles of the charge/discharge test. The dual-functional supercapacitor with a rapid and reversible response and high sustainability in optical modulation (96%) even under high current charge/discharge conditions is promising for real applications.

Received 15th November 2021
Accepted 21st January 2022

DOI: 10.1039/d1ta09795d

rsc.li/materials-a

1 Introduction

To fulfill the urgent demand for high-power sources, supercapacitors are known to be the most significant energy storage systems. Latest advancements in this field have proven the inclusion of different functionalities into supercapacitors, resulting in materials that are self-protective, stretchy, self-healing, colour-tunable, and self-charging.¹ Recently, integrating electrochromic functionality in supercapacitor devices has allowed the recognition of multiple applications including intelligent display and energy sensing in smart windows.^{2,3} However, the greatest challenge is simultaneously achieving high electrochemical performance and the corresponding electrochromic response while retaining high flexibility, transparency and stability.⁴

The successful realization of these multifunctional devices is mainly concentrated on the development of transparent conductive electrodes^{5–7} (TCEs) which rely on the material selection, efficient assembling procedure and accurate identical performance like high capacitance, a fast switching response and high switching stability.⁸ Previously, the commonly utilized ITO coated electrode and other conductive materials including metal NWs, graphene and conducting polymers have faced limitations of low conductivity, poor capacitive behaviour, and low optical transmittance when establishing highly conductive and transparent networks.^{9–12} However, efficient assembling procedures with different structures and arrangements help to achieve high electrochemical performance and the corresponding electrochromic response while retaining high conductivity, transparency and stability under high flexibility conditions. In this regard, numerous assembling methods have been launched like fabricating PANI films with a loose structure by the cyclic voltammetric electrodeposition (CV-GS) technique,¹³ spin-coating Ag NWs and PEDOT:PSS layers to construct a hybrid transparent conductive electrode^{14,15} and depositing Ag grids on flexible electrodes,¹⁶ enabling great potential in flexible bifunctional electrodes. However, the complex procedure, low areal capacitance, high response time and low sustainability in optical modulation are still concerning issues. Furthermore, the bending conditions produce cracks in inorganic materials which damage the conductive network and

^aCenter for Stretchable Electronics and NanoSensors, Key Laboratory of Optoelectronic Devices and Systems of Ministry of Education and Guangdong Province, College of Physics and Optoelectronic Engineering, Shenzhen University, Shenzhen 518060, China. E-mail: zcpeng@szu.edu.cn

^bState Key Laboratory of Automotive Safety and Energy, Tsinghua University, Beijing 100084, China

^cShenzhen Institute of Artificial Intelligence and Robotics for Society (AIRS), Shenzhen 518129, China

† Electronic supplementary information (ESI) available. See DOI: 10.1039/d1ta09795d

result in degradation in the electrochemical performance.¹⁷ Recently, co-assembly of different NWs by NW manipulation methods into macroscopic-scale structures would precisely tailor the conductivity of the flexible electrodes while balancing the optical transmittance.^{18,19} The electrode exhibited excellent mechanical stability, high conductivity, and transparency. However, the aforementioned NW electrode itself reveals comparatively poor electrochemical behaviour.¹² As a result, combining transparent metal electrodes with efficient pseudocapacitive materials would be highly effective to develop flexible hybrid electrodes for energy storage sensing applications. So far, there are no reports on co-assembly of multiple NWs with pseudocapacitive materials to control the conductivity and tuneable transparent properties of an electrode for supercapacitor applications.

Many pseudocapacitive materials like MnO_2 and RuO_x exhibit high charge storage and energy density. However, the stability of electrodes is a major issue and stability is always desired to deliver high energy density.^{20,21} As compared to these pseudocapacitive materials tungsten oxide (WO_x) nanostructures have been reported for charge storage *via* ion intercalation into the crystalline network with no compromise on structural integrity.^{22,23} Among the various WO_x nanostructures, the monoclinic $\text{W}_{18}\text{O}_{49}$ nanostructure is recognized as a viable electrode material for the future energy storage device, due to its availability of oxygen-vacancies for electrical conductivity.²⁴ Most significantly, it exhibits a distinct crystal structure that qualifies it as a viable host material for the ion intercalation process.²⁵ Additionally, $\text{W}_{18}\text{O}_{49}$ NW composites with carbonaceous materials like graphene have presented improved electrochemical properties due to a large surface area, high electrical conductivity and superior electrochemical stability which results in an improvement in the composite's electrochemical performance by accelerating ion diffusion and charge transfer.^{26,27} Comparing the electrochemical properties of the $\text{W}_{18}\text{O}_{49}$ NWs/rGO composite with a WO_x composite like WO_3 nanorods/graphene in previous reports,^{26,28} the $\text{W}_{18}\text{O}_{49}$ NWs/rGO composite exhibited higher specific capacitance than the WO_3 nanorods/graphene composites. In addition, $\text{W}_{18}\text{O}_{49}$ exhibits a distinct crystal structure that qualifies it as a viable host material for the ion intercalation process.²⁵ The better charge storage properties are attributed to the high aspect ratio and more oxygen vacancies of $\text{W}_{18}\text{O}_{49}$ NWs, which provide a more efficient transport pathway for both electrons and ions from the longitudinal axis of 1D NWs than that of the WO_3 nanorods.

Herein, we introduce the NW (Ag NWs and $\text{W}_{18}\text{O}_{49}$ NWs) manipulation method to construct flexible, transparent, and conductive electrodes. To introduce the charge storage and electrochromic properties, various $\text{W}_{18}\text{O}_{49}$ NWs/rGO composite layers were assembled on the prefabricated conductive electrode to develop electrodes with tuneable transmittance (72–84%) at 550 nm and a sheet resistance of 23–39 $\Omega \text{ sq}^{-1}$. In this study, the strategy of combining transparent metal electrodes with efficient pseudocapacitive materials not only represents a synergistic way of compounding desirable conductive and transparent properties but also facilitates high electrochemical

performance and the corresponding electrochromic response. The as-fabricated electrode exhibits excellent areal capacitance properties (92 mF cm^{-2} at 2 mA cm^{-2}) with a fast and reversible colour fluctuation response to changes in stored energy levels even under high current charge/discharge conditions. Furthermore, the electrode shows excellent electrochromic performance with fast switching speeds (8 s for coloration and 8.45 s for bleaching) and brilliant stability during the fast coloration/bleaching cycles. For practical applications, a bifunctional electrochromic supercapacitor device is fabricated which shows superior electrochemical performance with outstanding cycling stability up to 4000 cycles, and excellent mechanical properties.

2 Results and discussions

Ag NWs with uniform diameter and a high aspect ratio are presented in Fig. S1.† Fig. S2.† shows the $\text{W}_{18}\text{O}_{49}$ NWs with a high aspect ratio confirmed by transmission electron microscopy (TEM) and X-ray diffraction (XRD) spectra. The $\text{W}_{18}\text{O}_{49}$ NWs/rGO composite was prepared by our previously reported method.²⁹ Fig. S3.† shows the TEM images of $\text{W}_{18}\text{O}_{49}$ NW/rGO composites with various rGO weight ratios (2, 8, and 16 wt%), containing a uniform assembly of $\text{W}_{18}\text{O}_{49}$ NWs on the surface of the rGO sheet. The Fourier transform infrared (FTIR) spectra presented in Fig. S4.† show the reduction of GO by the disappearance of the C=O stretching vibration peak and C–O (alkoxy) stretching peaks appearing at 1738 cm^{-1} and 1074 cm^{-1} respectively, and the presence of W=O and bridging oxygen (OWO) peaks, appearing in the region of 1000–500 cm^{-1} .³⁰ Furthermore, Fig. S5.† shows the XRD spectra of the $\text{W}_{18}\text{O}_{49}$ NW/rGO composite with different weight contents, exhibiting the preferential growth of the $\text{W}_{18}\text{O}_{49}$ crystals along the [010] direction and removal of a strong peak at 11.22°, corresponding to the (002) interlayer in the GO sheet. Further verification about the successful assembly of $\text{W}_{18}\text{O}_{49}$ NWs on the GO sheet was confirmed by X-ray photoelectron spectroscopy (XPS) analysis (Fig. S6(a–c)),† showing that the peaks related to C–C/C=C, C=O, C–O, and O–C=O bonds in GO disappeared after the accumulation of $\text{W}_{18}\text{O}_{49}$ NWs. Fig. S6c.† exhibits two peaks appearing at 35.6 eV and 37.9 eV which can be ascribed to $\text{W}4f_{7/2}$ and $\text{W}4f_{5/2}$, respectively, suggesting the +6-oxidation state of W with characteristic binding energies.³¹

The assembly scheme for the fabrication of the flexible transparent conductive electrode is presented in Fig. 1. Initially, PVP-coated Ag and $\text{W}_{18}\text{O}_{49}$ NWs were mixed in a DMF and CHCl_3 solution with the volume ratio of solvents as 2 : 1 and a mass ratio of 4 : 10 ($\text{W}_{18}\text{O}_{49}$ NWs : Ag NWs) (Fig. 1a). Afterward, the as-prepared NW mixture was co-assembled by using the Langmuir–Blodgett (LB) technique and transferred twice from the LB trough to the PET substrate in a perpendicular direction, resulting in a NW conductive network as presented in Fig. 1b. In the NW network, Ag NWs behaved as a conductive component and $\text{W}_{18}\text{O}_{49}$ NWs acted as nanoscale spacers for the separation of Ag NWs with tuneable distances.¹⁹ At last, for the fabrication of flexible transparent electrodes showing charge storage and also electrochromic properties for supercapacitor devices, the pre-synthesized $\text{W}_{18}\text{O}_{49}$ NW/rGO composite (Fig. 1c

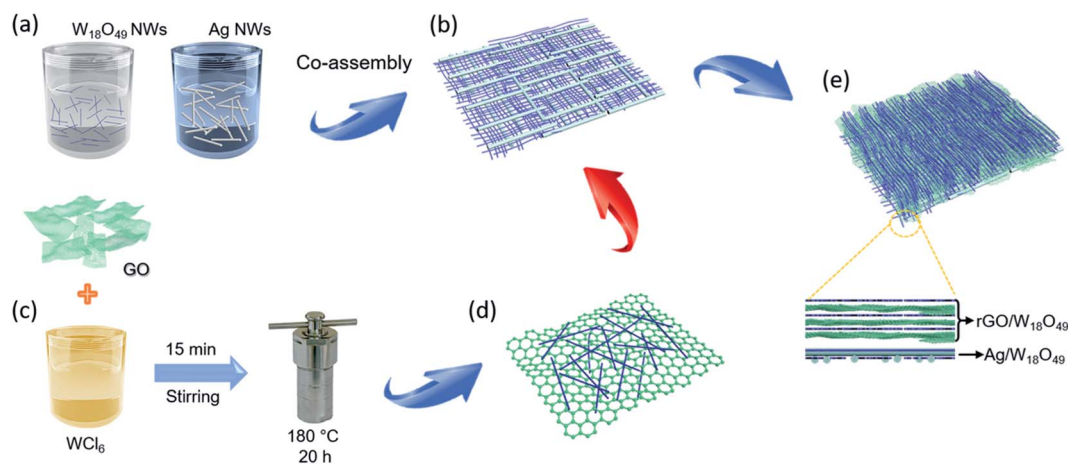


Fig. 1 Schematic explanation of flexible transparent W₁₈O₄₉ NWs/rGO composite film electrode fabrication. (a and b) Co-assembly of mixed NWs (W₁₈O₄₉ NWs and Ag NWs) by using the LB technique. (c and d) Synthesis of the W₁₈O₄₉ NW/rGO composite. (e) Assembly of the W₁₈O₄₉ NW/rGO composite on the prefabricated conductive electrode by using the LB method.

and d) was assembled on the transparent conductive electrodes by using an LB instrument (Fig. 1e). Transferring different layers (3, 5, 8, 10 and 15) of the assembled W₁₈O₄₉ NW/rGO composite will contribute more charge storage properties along with maintaining the transparency and electrochromic properties.

Fig. 2a shows the optical photographs of films with different W₁₈O₄₉ NW/rGO composite layers (3, 5, 8, 10 and 15). From the figure, we can find that the stripe pattern of the bottom layer can still be clearly observed through the electrode even at 15 layers, which proves that the electrode has good light transmittance. The distribution of Ag and W₁₈O₄₉ NWs in the perpendicular direction is confirmed by scanning electron microscopy (SEM), presented in Fig. 2b. The deposition of Ag NWs in the perpendicular direction results in a highly conductive and stable network. Also, W₁₈O₄₉ NWs control spacing between Ag NWs that helps to attain high transparency. At the same time, the film exhibited a high transparency of 88% at 550 nm (Fig. S7†). To confirm the presence of Ag and W₁₈O₄₉ NWs, we performed the XRD and EDS analyses of the Ag/W₁₈O₄₉ NW network electrode. The diffraction peaks at the 2θ value of 25° show the preferential growth of the W₁₈O₄₉ crystals along the [010] direction. Similarly, the peaks related to 38.3° and 44.5° could be indexed to the (111) and (200) reflections of face-centred-cubic (fcc) Ag (JCPDS no. 04-0783), respectively (Fig. S8†). The occurrence of peaks related to both elements confirmed the presence of Ag and W₁₈O₄₉ NWs in the electrode. Similarly, the EDS mapping also shows the presence of Ag and W elements in the electrode. The atomic percentage of Ag and W was estimated to be 71 and 28% respectively (Fig. S9(a-d)†).

Fig. 2c shows the SEM image of the assembly of the 15 layer 2 wt% W₁₈O₄₉ NW/rGO composite on the conductive electrode. Similarly, the deposition of the 8 wt% W₁₈O₄₉ NW/rGO composite is presented in Fig. S10,† showing high graphene content on the film. In addition, 15 layers of rGO, W₁₈O₄₉ NWs and the 2 wt% W₁₈O₄₉ NW/rGO composite show a corresponding film transparency of 74, 79 and 72% at the wavelength of 550

nm (Fig. 2d), indicating the small change in the transparency value when depositing 15 layers of W₁₈O₄₉ NW/rGO composite films. Moreover, the electrode transparency was also varied by increasing layers of the 2 wt% W₁₈O₄₉ NW/rGO composite. Fig. 2e indicates that by increasing the number of depositing layers from 3 to 15, the transparency of the electrode changed from 84 to 72% at 550 nm. However, depositing different layers of the 8 wt% W₁₈O₄₉ NW/rGO composite resulted in a decline in the transparency of the electrode as presented in Fig. S11.† At the same time, the sheet resistance of the electrode was also changed by depositing different layers (3, 5, 8, 10 and 15 layers) of 2 wt% W₁₈O₄₉ NW/rGO composite layers. Fig. 2f shows the gradual increase in thickness by increasing the number of deposited layers from 3 to 15 on a prefabricated Ag/W₁₈O₄₉ NW network. The Ag/W₁₈O₄₉ NW network itself has a thickness of 56 nm. By adding 3 layers of the W₁₈O₄₉ NWs/rGO composite, the thickness of the film changed from 56 to 90 nm. Furthermore, by increasing the number of deposited layers from 3 to 5, then to 8, 10 and 15, the total thickness (Ag/W₁₈O₄₉ NW network + W₁₈O₄₉ NWs/rGO composite) increased from 90 to 112, 155, 179 and 244 nm. So, the average thickness of each layer of the W₁₈O₄₉ NWs/rGO composite is 11–12 nm (Fig. S12†). However, the sheet resistance and transmittance both decreased from 39 to 23 $\Omega \text{ sq}^{-1}$ and from 84 to 72%, respectively. The decrease in sheet resistance was due to the increasing amount of rGO that was deposited on the electrode by increasing the number of layers. However, the transparency of the film declined due to the increasing amount of deposited materials by increasing the number of layers. As an excellent bifunctional electrode, the electrode must guarantee excellent conductivity while ensuring good light transmittance. Increasing the number of depositing layers beyond 15 resulted in a decline in transparency below 70%. Therefore, after comparison, we choose the electrode modified with a maximum of 15 layers of the W₁₈O₄₉ NW/rGO composite as the ideal electrode. To examine the mechanical stability of the flexible conductive electrode, a 6 cm long strip was bent to a radius of 1.5 cm and the resistance change was

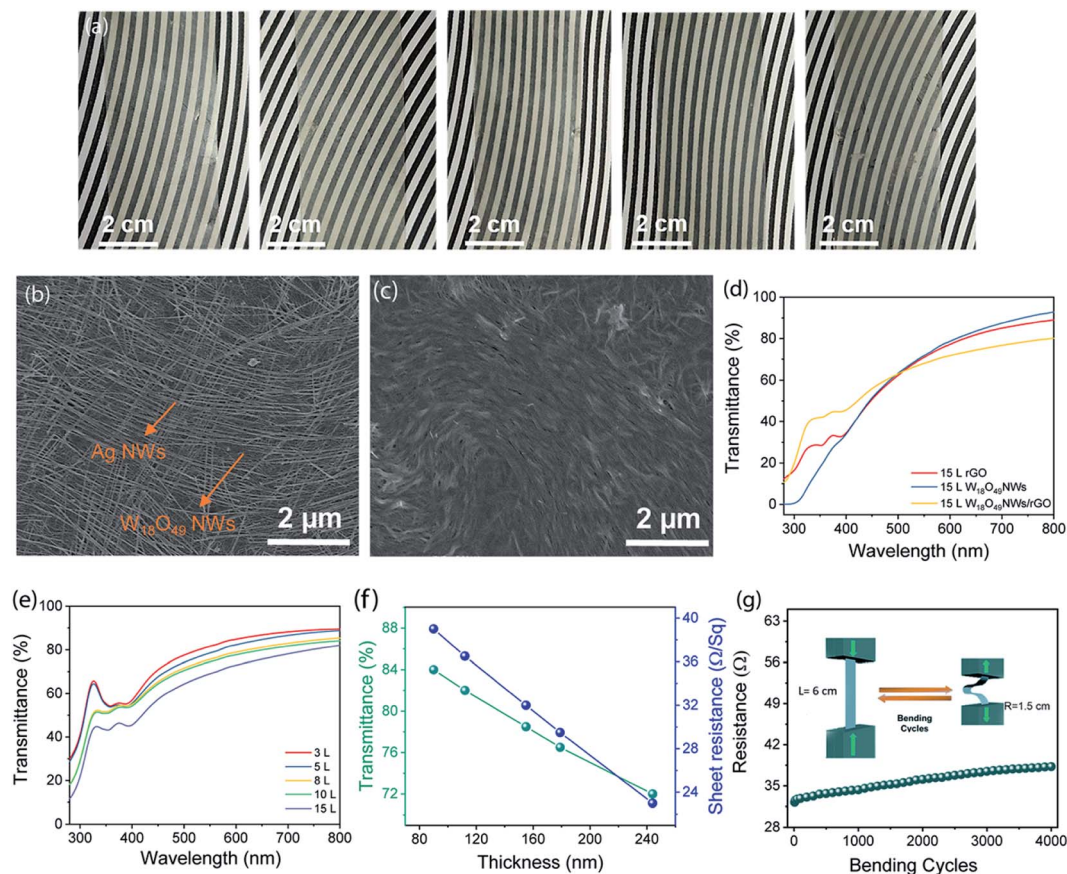


Fig. 2 (a) Photographs of the 3, 5, 8, 10 and 15 layers of the 2 wt% $W_{18}O_{49}$ NW/rGO composite deposited on a conductive PET substrate. (b) SEM image of Ag NWs and $W_{18}O_{49}$ NWs co-assembly (mAg : m $W_{18}O_{49}$, 10 : 4) on a PET substrate. (c) SEM photograph of 15 layers of the 2 wt% $W_{18}O_{49}$ NW/rGO composite assembled on the Ag/ $W_{18}O_{49}$ NW films. (d) Transmittance spectra for the flexible electrochromic film electrode comprising 15 layers of GO, $W_{18}O_{49}$ NWs and the $W_{18}O_{49}$ NW/rGO composite on a PET substrate, respectively. (e) Transmittance spectra for 3, 5, 8, 10 and 15 layers of the $W_{18}O_{49}$ NW/rGO composite deposited on a conductive PET substrate. (f) Thickness of the flexible electrode as a function of transmittance and sheet resistance of different layers (3, 5, 8, 10 and 15) of the $W_{18}O_{49}$ NW/rGO composite film. (g) Electrical resistance changes of the flexible electrode after 4000 bending cycles.

measured during the bending cycles. Fig. 2g shows a small resistance change during bending of the film electrode for 4000 bending cycles. The variation in the resistance of the electrode was calculated to be about 6.07Ω ($\Delta R/R \approx 15.7\%$), signifying brilliant mechanical stability under stress conditions.

The as-prepared flexible transparent electrodes with an effective area of $1.5 \times 1.5 \text{ cm}^2$ were tested in a three-electrode system using 0.5 M $AlCl_3$ aqueous electrolyte. Fig. 3a demonstrates the CV curves with pure rGO, $W_{18}O_{49}$ NWs and the 2 wt% $W_{18}O_{49}$ NW/rGO composite at 20 mV s^{-1} , clearly exhibiting the pseudocapacitive behaviour that was attributed to electrochemical reactions in the potential interval from -0.2 to 0.2 V . A significant escalation in the current density for the $W_{18}O_{49}$ NW/rGO composite electrode was detected as compared to rGO and the $W_{18}O_{49}$ NW electrode, demonstrating considerable higher areal capacitance for the $W_{18}O_{49}$ NW/rGO composite electrode. The large capacitance in the case of the $W_{18}O_{49}$ NW/rGO composite was attributed to the intimate electronic interaction between $W_{18}O_{49}$ NWs and rGO, simultaneously, accelerating electrochemical activity with effective and rapid conduction of charge carriers.²⁶ Moreover, these redox peaks can be ascribed

to the intercalation/deintercalation of Al^{3+} into the $W_{18}O_{49}$ NW/rGO structure *via* fast and reversible faradaic redox reactions, which contributes towards pseudocapacitive behaviour.^{32,33} To highlight the role of rGO in the $W_{18}O_{49}$ NW/rGO composite, CV curves of the 15 layer $W_{18}O_{49}$ NW/rGO composite electrode containing rGO in different weight contents (2 wt%, 8 wt% and 16 wt%) were measured at the same scan speed of 20 mV s^{-1} . Fig. S13[†] shows an increase in area under the CV curve by increasing the rGO content from 2 wt% to 8 wt% in the $W_{18}O_{49}$ NW/rGO composite, indicating higher charge storage properties in the case of 8 wt%. However, with increasing rGO content from 8 wt% to 16 wt%, the charge storage properties declined due to the lower reduction level of GO into rGO which impeded Al^{3+} diffusion and reduced Al^{3+} ion intercalation.²⁶ In addition, increasing the rGO content also reduced the transparency value of the electrode. Therefore, by balancing the transparency, the integral area of CV plots and the capacitance for these three samples including pure $W_{18}O_{49}$ NWs, 2 wt% and 8 wt% $W_{18}O_{49}$ NW/rGO composites, the 2 wt% $W_{18}O_{49}$ NW/rGO composite electrode was selected for further electrochemical discussion owing to better transparency and higher areal capacitance and

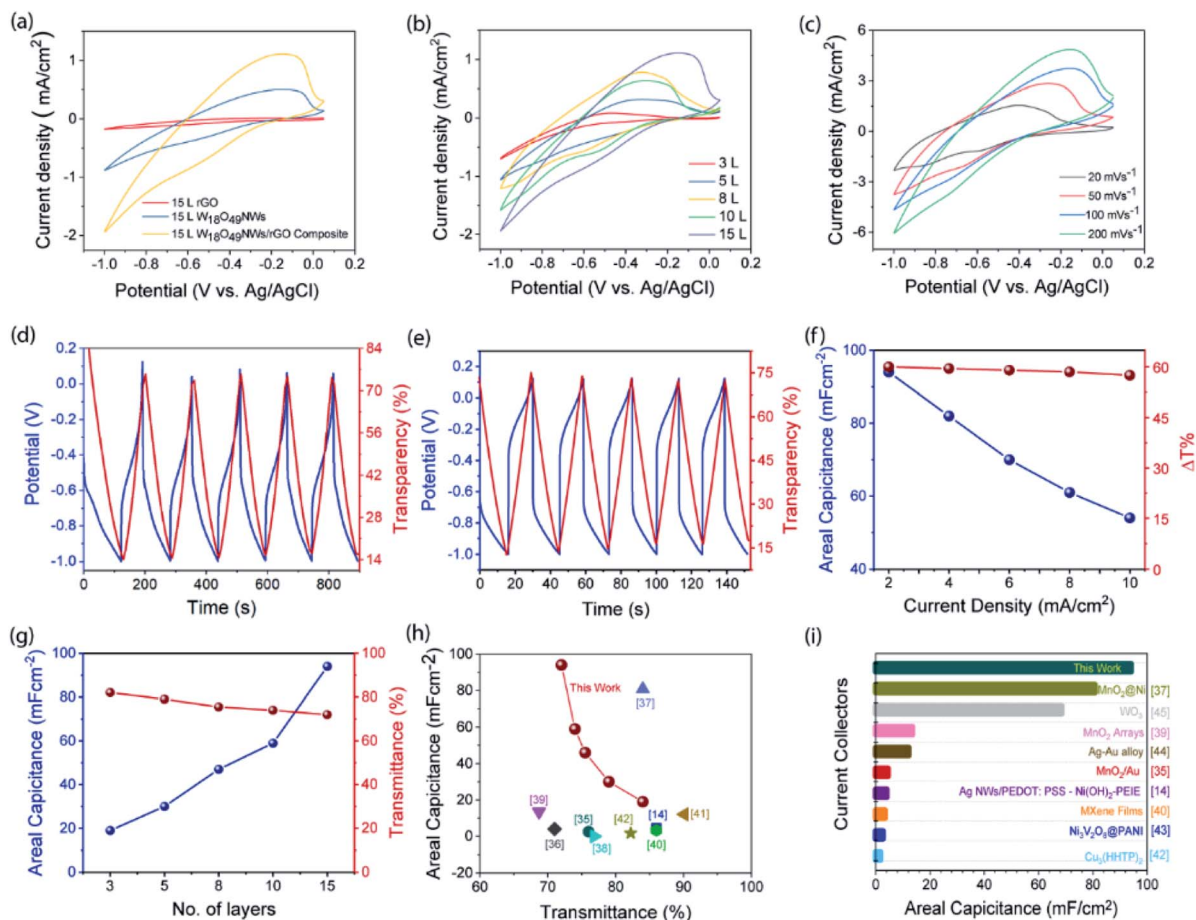


Fig. 3 (a) CV plots of 15 layers of rGO, $W_{18}O_{49}$ NWs and the 2 wt% $W_{18}O_{49}$ NW/rGO composite film electrode at 20 mV s^{-1} . (b) CV plots of different numbers of layers of the $W_{18}O_{49}$ NW/rGO composite film electrode at 20 mV s^{-1} . (c) Detailed CV plots of the 15 layer 2 wt% $W_{18}O_{49}$ NW/rGO composite film electrode at different scanning rates of 20, 50, 100 and 200 mV s^{-1} . (d) Galvanostatic charge/discharge curves at (d) 2 mA cm^{-2} and (e) 10 mA cm^{-2} in the potential range of -1 to 0.1 V and equivalent *in situ* optical responses at 633 nm for the 15 layer 2 wt% $W_{18}O_{49}$ NW/rGO composite film electrode. (f) Areal capacitance and optical modulation of the 15 layer 2 wt% $W_{18}O_{49}$ NW/rGO composite films as a function of the current density. (g) Areal capacitance and transmittance of the 2 wt% $W_{18}O_{49}$ NW/rGO composite films as a function of the number of layers. (h) Comparison of transmittance at a wavelength of 550 nm as a function of areal capacitance with other published literature on flexible transparent electrodes. (i) Comparison of areal capacitance as a function of other current collector thin films reported in previous literature.

could be an excellent candidate for the supercapacitor assembly. Also, CV curves with different numbers of layers (3, 5, 8, 10 and 15 layers) of the 2 wt% $W_{18}O_{49}$ NW/rGO composite electrode at 20 mV s^{-1} scanning rate are presented in Fig. 3b, showing broad redox peaks with an increasing number of layers, revealing the reversible redox reaction with excellent rate ability by increasing the number of layers of the $W_{18}O_{49}$ NW/rGO composite. Fig. 3c demonstrates the complete CV plots of 2 wt% $W_{18}O_{49}$ NW/rGO composite electrodes at different scanning rates of 20 mV s^{-1} , 50 mV s^{-1} , 100 mV s^{-1} and 200 mV s^{-1} , exhibiting the increase in current densities with a higher current rate and the ordered CV shape within the related potential range.

In addition, charge–discharge curves were measured at different current densities (2 to 10 mA cm^{-2}) in the potential range of -1 to 0.1 V and corresponding *in situ* transmittance was tested at 633 nm to determine electrochromic properties of the

electrode. Fig. 3d shows that during the charging process at the negative potential, the colour of the electrode turned deep blue, resulting in a decrease in transparency values. Similarly, the reverse discharging process resulted in the bleaching of the coloured electrode to a transparent state after discharging at 0.1 V . The colour change with the charging and discharging process was due to the efficient migration of Al^{3+} ions into $W_{18}O_{49}$ active sites thus generating fast and reversible redox reactions.^{8,16} To confirm the intercalation behaviour of the Al^{3+} ion, XRD of the hybrid electrode was performed at charged and discharged states (Fig. S14†). The electrode exhibited almost similar spectra in charged and discharged states. However, in the charged state, a small peak shift of the (010) peak was observed at a higher diffraction angle, indicating a decrease in interlayer spacing due to the electrostatic interaction of intercalated Al^{3+} ions with the polar atoms in the $W_{18}O_{49}$ structure, resulting in the d_{010} contraction. Similarly, in the discharged state, the (010) peak was

found to be at a lower diffraction angle, showing the d_{010} expansion by the de-intercalation of Al^{3+} ions during the discharging process.^{26,34} To evaluate the practicality, a high current charge–discharge process (10 mA cm^{-2}) and the corresponding *in situ* transmittances were recorded at 633 nm. A sufficient rapid colour change was observed in the electrode, signifying it as a potential candidate for the electrode in supercapacitor devices (Fig. 3e). Also, structural stability is important to evaluate the electrochemical performance of electrode materials. Therefore, to confirm the structural stability of the $\text{W}_{18}\text{O}_{49}$ NWs/rGO composite electrode during the electrochemical process, the morphology of electrode materials was determined before and after charging cycles by SEM analysis (Fig. S15†). No obvious change was observed in the morphology of materials showing the structural stability of the $\text{W}_{18}\text{O}_{49}$ NWs/rGO composite during the electrochemical process. In addition, XRD of the hybrid electrode confirmed similar spectra in charged and discharged states. However, a small peak shift of the (010) peak was observed at a higher diffraction angle due to Al^{3+} ion intercalation/deintercalation (Fig. S14†).

In addition, the relative dependence of areal capacitance and optical modulation on the current density was investigated. The electrode exhibited an areal capacitance from 92 to 54 mF cm^{-2} at changed current densities from 2 to 10 mA cm^{-2} (Fig. 3f). Meanwhile, with the increase of current density, as shown in Fig. 3f, the areal capacitance and optical modulation both decreased due to the inaccessibility of active surface areas of materials for charge storage, which restricted electroactive ion migration at high current density due to the diffusion effect.¹⁶ 58.6% of the initial areal capacitance and 94.7% of the initial optical modulation were retained at a current density of 10 mA

cm^{-2} , indicating an excellent rate capability under high current charge/discharge conditions. Also, increasing the number of layers of the 2 wt% $\text{W}_{18}\text{O}_{49}$ NW/rGO composite film from 3 to 15 resulted in an increase in capacitance from 19 mF cm^{-2} to 92 mF cm^{-2} at 2 mA cm^{-2} , however, transparency of the films declined from 84 to 72% as presented in Fig. 3g. A brief comparison of areal capacitance and transparency of the flexible transparent electrodes with previously published literature was established (Fig. 3h), revealing high tuneable transparency and exceptional areal capacitance as compared to other reported literature (Table S1†).^{14,35–42} Similarly, our material exhibited superior areal capacitance as compared to other electrode materials used in various thin-film systems (Fig. 3i).^{14,35,37,39,40,42–45}

In general, ideal electrochromic performance is characterized by four traditional parameters such as optical modulation, a low response time, a high coloration efficiency (CE) and high stability during the colour switching cycles. To illustrate the dynamic responses of electrodes briefly, electrochromic switching properties were measured. Fig. 4a shows the photograph of the coloured and bleached states of the electrode at different voltages. The UV-Vis spectra of the 15 layer $\text{W}_{18}\text{O}_{49}$ NW/rGO composite electrode in the coloured and bleached state were recorded, showing a major decline in transmittance of the film in the coloured state (Fig. 4b). The electrochromic switching cycles of different layered (3, 5, 8, 10 and 15 layers) $\text{W}_{18}\text{O}_{49}$ NW/rGO composite electrodes at the wavelength of 633 nm are presented in Fig. 4c, showing a gradual change in the colouring and fading properties with an applied voltage of 0 and -1 V . Also, from switching data, the response time (the time required for 90% of the optical change during the colouring or bleaching process)

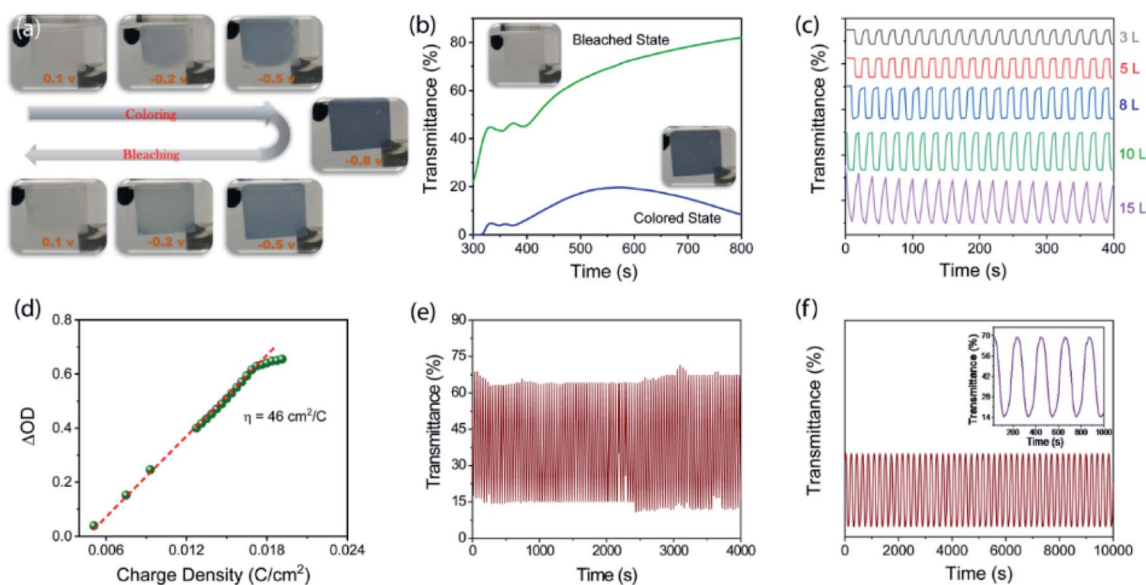


Fig. 4 (a) Photograph of the fabricated film electrode at different applied voltages. (b) Transmittance spectra of the 15 layer 2 wt% $\text{W}_{18}\text{O}_{49}$ NW/rGO composite film in the coloured and bleached state. (c) Electrochromic switching of the different layered (3, 5, 8, 10 and 15 layers) 2 wt% $\text{W}_{18}\text{O}_{49}$ NW/rGO composite film electrodes. (d) Optical density as a function of charge density. (e) Electrochromic switching of the 15 layer 2 wt% $\text{W}_{18}\text{O}_{49}$ NW/rGO composite films electrode for 4000 s. (f) Long-period electrochromic switching of the 15 layer 2 wt% $\text{W}_{18}\text{O}_{49}$ NW/rGO composite film electrode for 10 000 s.

was calculated. Fig. S16[†] shows the coloration and bleaching time of 3, 5, 8, 10 and 15 layer $W_{18}O_{49}$ NW/rGO composite films, revealing a responding hysteresis with the increased number of deposited layers. As shown in Fig. S16a,[†] the electrode with 3 layers of the $W_{18}O_{49}$ NW/rGO composite film revealed a fast colour-switching response of 2 s for colouring and 2.2 s for bleaching. When increased to 15 layers of the $W_{18}O_{49}$ NW/rGO composite film, the electrode exhibited a colouration time of 8 s and bleaching time of 8.25 s. Compared with previous reports, a faster switching time was observed from hexagonal tungsten oxide nanorod arrays (14 and 9 s) and NiO nanoparticles (11.5 and 9.5 s).^{8,46} The resulting fast switching time was attributed to the excellent contact between Ag and $W_{18}O_{49}$ NWs and strong electronic interaction between $W_{18}O_{49}$ NWs and rGO, consistent with previous reports.¹⁹

Another factor for evaluating the electrochromic performance is the coloration efficiency (η) which is primarily measured as the slope of the linear regime of the optical density fluctuation as a function of charge density. The coloration efficiency of the 15 layer $W_{18}O_{49}$ NW/rGO composite film was calculated to be $46 \text{ cm}^2 \text{ C}^{-1}$ as presented in Fig. 4d. To study the

switching stability, electrochromic switching cycles of the 15 layer $W_{18}O_{49}$ NW/rGO composite film electrode were tested for 4000 s, showing excellent sustainability of the optical modulation after 100 quick switching cycles (Fig. 4e), (Fig. S17[†]). The electrode maintained 96.41% of the original optical modulation after 100 cycles. To investigate the stability further, electrochromic switching cycles at low speed (230 s for one cycle) were tested for 10 000 s, indicating high stability and reversibility in cycles with a constant ΔT (Fig. 4f).

To explore the applications of these electrodes in portable transparent energy storage devices, fabrication of a flexible, transparent, and symmetric supercapacitor was carried out. From the obtained 15 layer 2 wt% $W_{18}O_{49}$ NW/rGO composite electrode, a symmetrical supercapacitor device was assembled with $AlCl_3$ electrolyte. Fig. 5a shows the fabrication scheme of a symmetrical supercapacitor device by sandwiching the $AlCl_3$ electrolyte between two identical 15 layer $W_{18}O_{49}$ NW/rGO composite electrodes. To confirm the merits of the as-fabricated flexible supercapacitor device, characterization studies including, cyclic voltammetry, galvanostatic charge/discharge with electrochromic switching cycles, and cycling stability

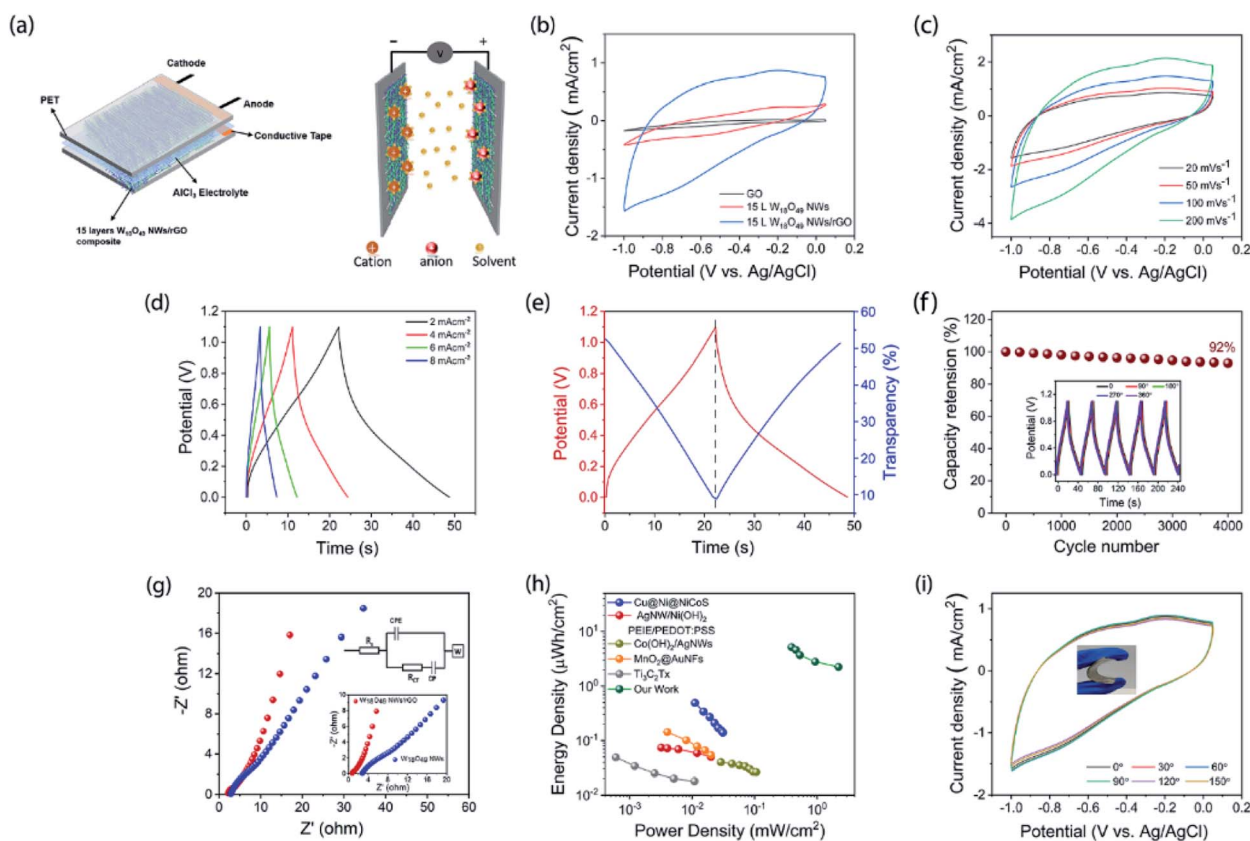


Fig. 5 (a) Schematic illustration of a symmetrical supercapacitor composed of identical 2 wt% $W_{18}O_{49}$ NW/rGO composite electrodes with $AlCl_3$ electrolyte. (b) CV plots of 15 layers, rGO, $W_{18}O_{49}$ NWs and the 2 wt% $W_{18}O_{49}$ NW/rGO composite film supercapacitor device at 20 mV s^{-1} . (c) CV plots of the 15 layer 2 wt% $W_{18}O_{49}$ NW/rGO composite film supercapacitor device at different scanning rates. (d) Galvanostatic charge/discharge curves at 2–8 mA cm^{-2} in the potential range of 0 to 1.1 V for the 15 layer $W_{18}O_{49}$ NW/rGO composite film supercapacitor device. (e) GCD curve at 2 mA cm^{-2} and the corresponding *in situ* transmittance profile at 633 nm for the supercapacitor device. (f) Long-term charge and discharge cycling stability of the symmetric supercapacitor device at 2 mA cm^{-2} . (g) Electrochemical impedance spectroscopy of symmetric supercapacitor devices (the insets show the fitted circuit diagram and magnified high-frequency region of the Nyquist plot). (h) Ragone plots of the symmetric supercapacitor device. (i) CV curves of the supercapacitor device under various bending angles at 20 mV cm^{-2} .

measurement were carried out. Fig. 5b presents the CV curves of rGO, $W_{18}O_{49}$ NWs and 2 wt% $W_{18}O_{49}$ NW/rGO composite symmetric supercapacitors at 20 mV s^{-1} with a potential interval from -0.2 to 0.2 V . The broad redox peaks appearing in the curves proposed the faradaic reactions occurring between the electrodes. Also, the large integral area appearing in the CV curves of the $W_{18}O_{49}$ NW/rGO composite film supercapacitors revealed higher areal capacitance as compared to pure rGO and $W_{18}O_{49}$ NW film supercapacitors. The accelerated electrochemical activity in the case of $W_{18}O_{49}$ NW/rGO composite supercapacitors was due to the large intimate electronic interaction between $W_{18}O_{49}$ NWs and rGO simultaneously. The CV plots for the 2 wt% $W_{18}O_{49}$ NW/rGO composite supercapacitor at different scanning rates (20 to 200 mV s^{-1}) are presented in Fig. 5c, showing a gradual increase in current density peaks with increased scanning speed while maintaining the CV shape. To further elucidate the electrochemical capacitance performance of the assembled supercapacitors, the charge and discharge curves were measured. Fig. 5d shows charging and discharging plots of the supercapacitor device at a current density of $2\text{--}8 \text{ mA cm}^{-2}$, suggesting sustainable capacitance in a broad current range. Similarly, charge–discharge properties at a current density of 2 mA cm^{-2} are presented in Fig. 5e with the corresponding *in situ* transmittance profile at 633 nm . The areal capacitances of the device are presented in Fig. S18,† showing an areal capacitance of 48 mF cm^{-2} at a current density of 2 mA cm^{-2} . The areal capacitance decreased from 48 to 20 mF cm^{-2} with increasing current densities from 2 to 8 mA cm^{-2} , indicating that 41.6% of the areal capacitance was maintained under a wide current density alteration. Moreover, along with areal capacitance, the device also maintained 96% of the optical modulation during the increase in current density from 2 mA cm^{-2} to 8 mA cm^{-2} (Fig. S18†). For practical applications, the cycling stability is considered an effective factor that was inferred under 4000 continuous charge/discharge cycles with the current density at 2 mA cm^{-2} (Fig. 5f), revealing excellent cycling stability while retaining 92.3% of its initial capacitance. To investigate the charge storage characteristics and electronic conductivity, electrochemical impedance spectroscopy (EIS) of the $W_{18}O_{49}$ NW symmetrical supercapacitor and $W_{18}O_{49}$ NW/rGO composite symmetrical supercapacitors was conducted from 100 kHz to 0.01 Hz (Fig. 5g). Prominently, the almost vertical shape of the Nyquist plots with a steeper slope was observed in the low-frequency region, suggesting the excellent capacitive actions of the supercapacitor devices. The fitted circuit with Nyquist curves (inset of the figure) revealed the solution resistance of $W_{18}O_{49}$ NWs and $W_{18}O_{49}$ NW/rGO composite symmetrical supercapacitors to be around 3.28 and 2.5Ω , respectively. Similarly, the $W_{18}O_{49}$ NW/rGO composite supercapacitor exhibited a good conduction rate of the charge carriers compared to the pure $W_{18}O_{49}$ NW supercapacitor and it showed a charge transfer resistance of 245Ω , while the $W_{18}O_{49}$ NWs exhibited a resistance of 299Ω . Moreover, the $W_{18}O_{49}$ NW/rGO composite supercapacitors also exhibited a smaller Warburg resistance as compared to $W_{18}O_{49}$ NWs, due to ease of charge transfer during the intercalation of Al^{3+} ions, which was most likely due to the inclusion of rGO in the $W_{18}O_{49}$ NW/rGO composite film.

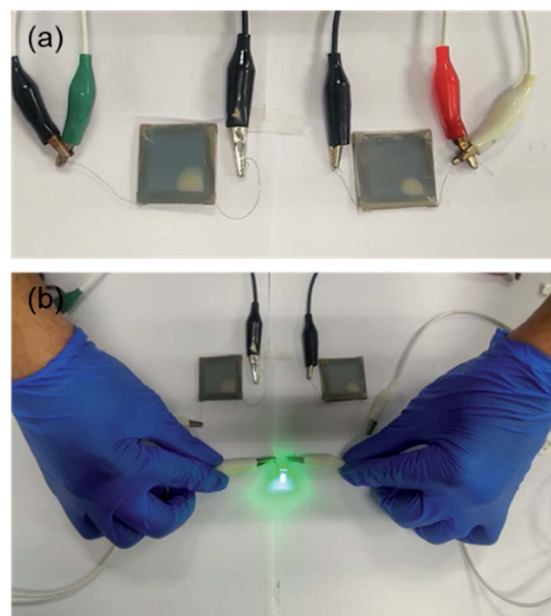


Fig. 6 Photographs of the supercapacitor device during the (a) charging of the supercapacitor device and (b) connection with an LED to turn it ON.

For the practical evaluation of the fabricated supercapacitor, the energy density and power density of the total device were calculated. The specific Ragone plot presented in Fig. 5h depicted a maximum energy density of $5.2 \mu\text{W h cm}^{-2}$ at a power density of 0.391 mW cm^{-2} . The device also maintained an energy density of $2.25 \mu\text{W h cm}^{-2}$ even at a maximum power density of 2.21 mW cm^{-2} . In addition, while compared to other reported literature, our device revealed higher energy densities ($2.25\text{--}5.2 \mu\text{W h cm}^{-2}$)^{14,38,47–49} as shown in Fig. 5h and Table S2.† The flexibility evaluation of the symmetrical supercapacitor device was conducted by using the CV measurement (scan speed, 20 V s^{-1}) under different bending angles. From Fig. 5i, no obvious change in capacitance was observed by changing the bending angle of the device from 0° to 150° , revealing excellent mechanical flexibility of the supercapacitor device. The inset photograph also confirmed the flexibility of the device.

To demonstrate the practical device application, the supercapacitor device was fabricated by sandwiching the $AlCl_3$ electrolyte between two identical $W_{18}O_{49}$ NW/rGO composite electrodes (Fig. 6a and b). The resulting supercapacitor devices were connected in series and successfully functioned as both an energy storage device and electrochemical reflective display. On charging the device exhibited deep blue colour. To detect the employment of the charged energy, the supercapacitor device was connected to a green light-emitting diode (LED), turning ON the LED light as presented in Fig. 6b.

3 Conclusions

In this study, highly flexible, transparent electrodes were fabricated by depositing flexible $Ag/W_{18}O_{49}$ NW films using the NW manipulation method, followed by the deposition of

multiple $W_{18}O_{49}$ NWs/rGO composite layers. The electrodes exhibited high conductivity with tuneable resistances ($23\text{--}39\ \Omega\ \text{sq}^{-1}$) and transmittance ($72\text{--}84\%$ at $550\ \text{nm}$) while maintaining their functionalities after 4000 bending cycles. A large areal capacitance ($92\ \text{mF cm}^{-2}$) with a fast and reversible switching response was attained. The electrode can sustain high optical modulation even under high current charge/discharge conditions. Furthermore, excellent stability was achieved during the colour switching cycles. A smart supercapacitor based on the hybrid transparent electrodes was demonstrated, which can recognize the level of stored energy with reversible colour change. The device showed excellent mechanical flexibility and stability up to 4000 charge/discharge cycles. With the significantly enhanced performance, the hybrid film electrode can also find potential applications in other flexible electronics and human-machine interfaces.

4 Experimental

4.1 Synthesis of Ag NWs

In a standard synthesis method, 1 g PVP ($M_w \approx 37\ 000$) was added into 40 mL glycerol in a three-necked flask and heated in an oil bath at $60\ ^\circ\text{C}$ for 30 minutes under magnetic stirring. After the complete dissolution of PVP, the three-necked flask was transferred into an ice water bath until the temperature of the solution decreased to $40\ ^\circ\text{C}$. Then 0.3 mL (0.5 g) of aqueous AgNO_3 and 0.2 mL (30 mg) of aqueous NaCl solution was injected under continuous stirring and the reaction mixture was transferred to a 50 mL autoclave and heated in a $180\ ^\circ\text{C}$ oven for 16 h. Upon completion of the reaction, the autoclave was removed from the oven and cooled to room temperature. After sedimentation for 48 h, the upper suspension was poured out and deposited Ag NWs were obtained. The conversion rate was 74.8% with a concentration of $5.925\ \text{mg mL}^{-1}$.

4.2 Synthesis of $W_{18}O_{49}$ /rGO composites

The $W_{18}O_{49}$ NWs/rGO composites were prepared by modifying our previously reported method. In a detailed procedure, 30 mg of WCl_6 salt and 2 mg of PVP were dissolved in 20 mL ethanol to attain a yellow solution. Similarly, GO solution was prepared by adding different amounts of GO in 20 mL ethanol separately and mixing with WCl_6 solution with continuous stirring for 10 minutes. The obtained mixtures in weight ratios of 2, 8 and 16 wt% were moved into a PTFE-lined 50 mL autoclave and kept at $180\ ^\circ\text{C}$ for 20 h. Upon completion of the reaction, the obtained reaction mixtures were cooled and purified by washing with water and ethanol *via* centrifugation at 4000 rpm for 5 min.

4.3 Fabrication of transparent electrochromic films

A highly organized network comprising Ag NWs and $W_{18}O_{49}$ NWs was fabricated by using an improved Langmuir-Blodgett (LB) technique. The pre-washed Ag NWs ($3\ \text{mg mL}^{-1}$) and $W_{18}O_{49}$ NW ($0.6\ \text{mg mL}^{-1}$) solutions were prepared separately in a solvent mixture of 0.75 mL of *N,N*-dimethylformamide (DMF) solution and 0.5 mL of chloroform (CHCl_3) and then mixed to form a homogenous dispersion with a volume ratio of

1 : 2. The dispersion of NW solution of the LB trough was carried out by using a syringe followed by compression at a rate of $20\ \text{cm}^2\ \text{min}^{-1}$ to align the NWs. By depositing aligned NWs in a perpendicular direction on a PET substrate, a transparent film was obtained comprising a network of NWs. To further control the charge storage with electrochromic properties, different $W_{18}O_{49}$ NW/rGO composite layers were deposited by using LB technology and transferred to the Ag/ $W_{18}O_{49}$ NW network.

4.4 Electrochemical measurements

To test the performance of the supercapacitor, a three electrode system was applied. Cyclic voltammetry (CV) and galvanic charge-discharge tests were carried out to evaluate the electrochemical properties of the electrode. From these tests, the areal capacitance of the electrode was determined by using the following formula:

$$C_a = \frac{I\Delta t}{A\Delta V} \quad (1)$$

where I is the discharge current (mA), Δt is the discharge time (s), A is the geometrical area of the electrode (cm^2), and ΔV is the potential window (V).

Similarly, from the charge-discharge tests, the areal capacitance of the supercapacitor device was calculated by using the following formula:

$$C_a = 2 \times \frac{I\Delta t}{A\Delta V} \quad (2)$$

The energy density (E) in $\mu\text{Wh cm}^{-2}$ and the power density (P) in mW cm^{-2} of the supercapacitor device is attained by using the following equations:⁴³

$$E_a = \frac{C_a(\Delta V)^2 \times 1000}{2 \times 3600} \quad (3)$$

$$P = \frac{3600 \times E_a}{\Delta t \times 1000} \quad (4)$$

where C_a is the areal capacitance (mF cm^{-2}) of the device, ΔV is the total potential window, and Δt is the discharge time.

Coloration efficiency (CE). Another significant factor of an electrochromic material is the CE that can be calculated by using the following equations:

$$\text{CE} = \frac{\Delta\text{OD}}{Q} \quad (5)$$

where ΔOD the optical density is presented as:

$$\Delta\text{OD} = \log \frac{T_b}{T_c} \quad (6)$$

where Q presents the charge density (C cm^{-2}), and T_b and T_c are the transmittance of the bleached and coloured states, respectively.

4.5 Device characterization

Scanning electron microscopy (SEM) was carried out with a Zeiss Supra 40 scanning electron microscope at 5 kV

acceleration voltage. The X-ray diffraction patterns (XRD) were measured on a Philips X'Pert Pro Super X-ray diffractometer equipped with graphite-monochromatized Cu KR radiation. UV-vis spectra were recorded on a UV-2501PC/2550 at room temperature. The electrical resistance and mechanical stability of the devices were tested by using a Keithley 4200 SCS and a mechanical system (Instron 5565A). Electrochemical measurements were carried out using a three-electrode system on an IM6ex electrochemical workstation (Zahner, Germany).

Author contributions

MH and ZP conceived the idea. MH and GM carried out the experiments and analysis. MH, YL, ZW wrote the original manuscript. ZP supervised the project and edited the manuscript.

Conflicts of interest

There are no conflicts to declare.

Acknowledgements

This work was supported in part by the Science and Technology Innovation Commission of Shenzhen under grants KQTD20170810105439418 and JCYJ20200109114237902, in part by the joint funding program of the Guangdong Department of Science and Technology and Hongkong Innovation and Technology Fund under grant 2021A0505110015, and the funding from the Shenzhen Institute of Artificial Intelligence and Robotics for Society (AC01202101011).

References

- 1 F. X. Wang, X. W. Wu, X. H. Yuan, Z. C. Liu, Y. Zhang, L. J. Fu, Y. S. Zhu, Q. M. Zhou, Y. P. Wu and W. Huang, *Chem. Soc. Rev.*, 2017, **46**, 6816–6854.
- 2 K. Wang, H. Wu, Y. Meng, Y. Zhang and Z. Wei, *Energy Environ. Sci.*, 2012, **5**, 8384–8389.
- 3 Q. Liu, G. Zhang, N. Chen, X. Feng, C. Wang, J. Wang, X. Jin and L. Qu, *Adv. Funct. Mater.*, 2020, **30**, 2002086.
- 4 Y.-H. Lee, J. S. Kang, J.-H. Park, J. Kang, I.-R. Jo, Y.-E. Sung and K.-S. Ahn, *Nano Energy*, 2020, **72**, 104720.
- 5 D. Li, W. Y. Lai, Y. Z. Zhang and W. Huang, *Adv. Mater.*, 2018, **30**, 1704738.
- 6 L. Zhou, M. Yu, X. Chen, S. Nie, W. Y. Lai, W. Su, Z. Cui and W. Huang, *Adv. Funct. Mater.*, 2018, **28**, 1705955.
- 7 T. Cheng, Y.-Z. Zhang, J.-P. Yi, L. Yang, J.-D. Zhang, W.-Y. Lai and W. Huang, *J. Mater. Chem. A*, 2016, **4**, 13754–13763.
- 8 X. Huo, X. Miao, X. Han, S. Tang, M. Zhang and M. Guo, *J. Mater. Chem. A*, 2020, **8**, 9927–9938.
- 9 T. Chen, Y. Xue, A. K. Roy and L. Dai, *ACS Nano*, 2014, **8**, 1039–1046.
- 10 P. Kanninen, N. D. Luong, I. V. Anoshkin, A. Tsapenko, J. Seppälä, A. G. Nasibulin and T. Kallio, *Nanotech*, 2016, **27**, 235403.
- 11 H. Wu, D. Kong, Z. Ruan, P.-C. Hsu, S. Wang, Z. Yu, T. J. Carney, L. Hu, S. Fan and Y. Cui, *Nat. Nanotechnol.*, 2013, **8**, 421–425.
- 12 H. Lee, S. Hong, J. Lee, Y. D. Suh, J. Kwon, H. Moon, H. Kim, J. Yeo and S. H. Ko, *ACS Appl. Mater. Interfaces*, 2016, **8**, 15449–15458.
- 13 K. Zhou, H. Wang, J. Jiu, J. Liu, H. Yan and K. Suganuma, *Chem. Eng. J.*, 2018, **345**, 290–299.
- 14 R. T. Ginting, M. M. Ovhall and J.-W. Kang, *Nano Energy*, 2018, **53**, 650–657.
- 15 X. Liu, D. Li, X. Chen, W.-Y. Lai and W. Huang, *ACS Appl. Mater. Interfaces*, 2018, **10**, 32536–32542.
- 16 G. Cai, P. Darmawan, M. Cui, J. Wang, J. Chen, S. Magdassi and P. S. Lee, *Adv. Energy Mater.*, 2016, **6**, 1501882.
- 17 R. Singh, J. Tharion, S. Murugan and A. Kumar, *ACS Appl. Mater. Interfaces*, 2017, **9**, 19427–19435.
- 18 J.-L. Wang, J.-W. Liu, S.-Z. Sheng, Z. He, J. Gao and S.-H. Yu, *Nano Lett.*, 2021, **21**, 9203–9209.
- 19 J.-L. Wang, Y.-R. Lu, H.-H. Li, J.-W. Liu and S.-H. Yu, *J. Am. Chem. Soc.*, 2017, **139**, 9921–9926.
- 20 X. Sun, T. Xu, J. Bai and C. Li, *ACS Appl. Energy Mater.*, 2019, **2**, 8675–8684.
- 21 J. B. Cook, T. C. Lin, H.-S. Kim, A. Siordia, B. S. Dunn and S. H. Tolbert, *ACS Nano*, 2019, **13**, 1223–1231.
- 22 J. B. Mitchell, N. R. Geise, A. R. Paterson, N. C. Osti, Y. Sun, S. Fleischmann, R. Zhang, L. A. Madsen, M. F. Toney, D.-e. Jiang, A. I. Kolesnikov, E. Mamontov and V. Augustyn, *ACS Energy Lett.*, 2019, **4**, 2805–2812.
- 23 V. Augustyn, J. Come, M. A. Lowe, J. W. Kim, P.-L. Taberna, S. H. Tolbert, H. D. Abruna, P. Simon and B. Dunn, *Nat. Mater.*, 2013, **12**, 518–522.
- 24 X. Zhong, Y. Sun, X. Chen, G. Zhuang, X. Li and J. G. Wang, *Adv. Funct. Mater.*, 2016, **26**, 5778–5786.
- 25 S. Cong, F. Geng and Z. Zhao, *Adv. Mater.*, 2016, **28**, 10518–10528.
- 26 M. R. Thalji, G. A. M. Ali, P. Liu, Y. L. Zhong and K. F. Chong, *Chem. Eng. J.*, 2021, **409**, 128216.
- 27 K. R. Li, Y. L. Shao, S. Y. Liu, Q. H. Zhang, H. Z. Wang, Y. G. Li and R. B. Kaner, *Small*, 2017, **13**, 10.
- 28 X. h. Guan, Z. w. Zhang, L. Yang and G. s. Wang, *ChemPlusChem*, 2017, **82**, 1174–1181.
- 29 M. Hassan, Z.-H. Wang, W.-R. Huang, M.-Q. Li, J.-W. Liu and J.-F. Chen, *Sensors*, 2017, **17**, 2245.
- 30 A. Tocchetto and A. Glisenti, *Langmuir*, 2000, **16**, 6173–6182.
- 31 G. Xi, S. Ouyang, P. Li, J. Ye, Q. Ma, N. Su, H. Bai and C. Wang, *Angew. Chem., Int. Ed.*, 2012, **51**, 2395–2399.
- 32 V. Augustyn, J. Come, M. A. Lowe, J. W. Kim, P.-L. Taberna, S. H. Tolbert, H. D. Abruña, P. Simon and B. Dunn, *Nat. Mater.*, 2013, **12**, 518–522.
- 33 J. Yan, C. E. Ren, K. Maleski, C. B. Hatter, B. Anasori, P. Urbankowski, A. Sarycheva and Y. Gogotsi, *Adv. Funct. Mater.*, 2017, **27**, 1701264.
- 34 K. Li, Y. Shao, H. Yan, Z. Lu, K. J. Griffith, J. Yan, G. Wang, H. Fan, J. Lu, W. Huang, B. Bao, X. Liu, C. Hou, Q. Zhang, Y. Li, J. Yu and H. Wang, *Nat. Commun.*, 2018, **9**, 1–11.

- 35 K.-W. Kim, T. Y. Yun, S.-H. You, X. Tang, J. Lee, Y. Seo, Y.-T. Kim, S. H. Kim, H. C. Moon and J. K. Kim, *NPG Asia Mater.*, 2020, **12**, 1–10.
- 36 Y. Lee, S. Chae, H. Park, J. Kim and S.-H. Jeong, *Chem. Eng. J.*, 2020, **382**, 122798.
- 37 Y.-H. Liu, J.-L. Xu, X. Gao, Y.-L. Sun, J.-J. Lv, S. Shen, L.-S. Chen and S.-D. Wang, *Energy Environ. Sci.*, 2017, **10**, 2534–2543.
- 38 B. S. Soram, I. S. Thangjam, J. Y. Dai, T. Kshetri, N. H. Kim and J. H. Lee, *Chem. Eng. J.*, 2020, **395**, 125019.
- 39 Y. Wang, W. Zhou, Q. Kang, J. Chen, Y. Li, X. Feng, D. Wang, Y. Ma and W. Huang, *ACS Appl. Mater. Interfaces*, 2018, **10**, 27001–27008.
- 40 D. Wen, X. Wang, L. Liu, C. Hu, C. Sun, Y. Wu, Y. Zhao, J. Zhang, X. Liu and G. Ying, *ACS Appl. Mater. Interfaces*, 2021, **13**, 17766–17780.
- 41 H. Zhang, Y. Tian, S. Wang, Y. Huang, J. Wen, C. Hang, Z. Zheng and C. Wang, *Chem. Eng. J.*, 2020, **399**, 125075.
- 42 W. Zhao, T. Chen, W. Wang, S. Bi, M. Jiang, K. Y. Zhang, S. Liu, W. Huang and Q. Zhao, *Adv. Mater. Interfaces*, 2021, **8**, 2100308.
- 43 X. Liu, J. Wang and G. Yang, *ACS Appl. Mater. Interfaces*, 2018, **10**, 20688–20695.
- 44 H. Zhang, Y. Tian, S. Wang, Y. Huang, J. Wen, C. Hang, Z. Zheng and C. Wang, *Chem. Eng. J.*, 2020, **399**, 125075.
- 45 J. Chen, Z. Wang, Z. Chen, S. Cong and Z. Zhao, *Nano Lett.*, 2020, **20**, 1915–1922.
- 46 G. Cai, X. Wang, M. Cui, P. Darmawan, J. Wang, A. L.-S. Eh and P. S. Lee, *Nano Energy*, 2015, **12**, 258–267.
- 47 H. Sheng, X. Zhang, Y. Ma, P. Wang, J. Zhou, Q. Su, W. Lan, E. Xie and C. J. Zhang, *ACS Appl. Mater. Interfaces*, 2019, **11**, 8992–9001.
- 48 S. B. Singh, T. I. Singh, N. H. Kim and J. H. Lee, *J. Mater. Chem. A*, 2019, **7**, 10672–10683.
- 49 C. Zhang, B. Anasori, A. Seral-Ascaso, S.-H. Park, N. McEvoy, A. Shmeliov, G. S. Duesberg, J. N. Coleman, Y. Gogotsi and V. Nicolosi, *Adv. Mater.*, 2017, **29**, 1702678.